Growth of 1D TiO_2 Nanostructures on Ti Substrates Incorporated with Residual Stress through Humid Oxidation and their Characterizations

M. M. Arafat[1], B. Dinan[2], A. S. M. A. Haseeb[3], S. A. Akbar[2], B. M. A. Rahman[4], S. Rozali[3], S. Naher[1]

M. M. Arafat
Department of Mechanical Engineering and Aeronautics
School of Mathematics, Computer Science and Engineering
City University of London, Northampton Square, London EC1V 0HB, United Kingdom.
E-Mail: arafat.mahmood@city.ac.uk; arafat_mahmood@yahoo.com

B. Dinan
Department of Materials Science and Engineering
Ohio State University, 2041 College Road, Columbus, OH 43210, USA.
E-Mails: dinan@matsceng.ohio-state.edu

A. S. M. A. Haseeb
Department of Mechanical Engineering
Faculty of Engineering, University of Malaya, 50603 Kuala Lumpur, Malaysia.
E-Mail: haseeb@um.edu.my

S. A. Akbar
Department of Materials Science and Engineering
Ohio State University, 2041 College Road, Columbus, OH 43210, USA.
E-Mails: akbar.1@osu.edu

B. M. A. Rahman
Department of Electrical and Electronic Engineering
School of Mathematics, Computer Science and Engineering
City University of London, Northampton Square, London EC1V 0HB, United Kingdom.
Email: b.m.a.rahman@city.ac.uk

S. Rozali

Department of Mechanical Engineering

Faculty of Engineering

University of Malaya, 50603 Kuala Lumpur, Malaysia.

E-Mail: azuar@um.edu.my

S. Naher

Department of Mechanical Engineering and Aeronautics

School of Mathematics, Computer Science and Engineering

City University of London, Northampton Square, London EC1V 0HB, United Kingdom.

Email: sumsun.naher.1@city.ac.uk

Abstract

Different Ti substrates, such as particles (as-received and ball milled), plate and TEM grid were oxidized for the growth of 1D TiO_2 nanostructures. The Ti substrates were oxidized for 4 h at temperatures of 700-750 °C in humid and dry Ar containing 5 ppm of O_2. The effects of residual stress on the growth of 1D TiO_2 nanostructures were investigated. The residual stress inside the Ti particles was measured by XRD-$\sin^2\psi$ technique. The oxidized Ti substrates were characterized using field emission scanning electron microscope (FESEM) equipped with energy dispersive X-ray (EDX) spectroscope, transmission electron microscope (TEM), X-ray diffractometer (XRD) and X-ray photoelectron spectroscope (XPS). Results revealed that humid environment enhances the growth of 1D TiO_2 nanostructures. Four different types of 1D morphologies obtained during humid oxidation, e.g., stacked, ribbon, plateau and lamp-post shaped nanostructures. The presence of residual stress significantly enhances the density and coverage of 1D nanostructures. The as-grown TiO_2 nanostructures possess tetragonal rutile structure having length up to 10 µm along the <1 0 1> directions. During initial stage of oxidation, a TiO_2 layer is first formed on Ti substrate. Lower valence oxides (Ti_3O_5, Ti_2O_3 and TiO) then form underneath the TiO_2 layer and induce stress at the interface of oxide layers. The induced stress plays significant role on the growth of 1D TiO_2 nanostructures. The induced stress is relaxed by creating new surfaces in the form of 1D TiO_2 nanostructures. A diffusion based model is proposed to explain the mechanism of 1D TiO_2 growth during humid oxidation of Ti. The 1D TiO_2 nanostructures and TiO_2 layer is formed by the interstitial diffusion of Ti^{4+} ions to the surface and reacts with the surface adsorbed hydroxide ions (OH^-). Lower valence oxides are formed at the metal-oxide interface by the reaction between diffused oxygen ions and Ti ions.

Keywords

Ti substrates; TiO_2 nanostructures; 1D nanostructures; Thermal oxidation; Humid oxidation; Rutile

1. Introduction

Over the past few decades, nanostructured metal oxides have been of great scientific interest among researchers, engineers and industrialists due to their unique chemical and physical properties, such as dimensional characteristics [1-3], enhanced surface area [4, 5], quantum confinement [6, 7] and superior electrical properties [8-10]. These characteristics of nanostructured materials are significantly different from their bulk counterparts. For these reasons, the research focusing on the fabrication, characterizations and applications of nanostructured materials in the field of electronics, optoelectronics and electro-mechanical devices have gained prominence [11].

The wide direct band gap (3-3.2 eV), non-toxicity, high temperature stability, low production cost and outstanding physical, chemical and optical properties fueled the research interest towards nanostructured TiO_2 in various applications [12]. A rich family of TiO_2 based nanomaterials, such as zero dimensional (0D), one dimensional (1D), two dimensional (2D), and three dimensional (3D) nanostructures have been synthesized and their properties have been explored. Out of these, nanostructures of 1D TiO_2 have been extensively studied due to having numerous applications in many engineering fields including dye-sensitized solar cells [13, 14], photo-detector [15, 16], photo-catalyst [17-19], photo-splitting of water [20-22], photo-electrochemical cells [23, 24], gas sensors [25, 26], piezo-electronics [27], super capacitors [28], lithium ion batteries [29, 30], field emitters [31, 32], and bone implantation [33, 34].

Researchers invented many sophisticated and innovative processing routes, such as hydrothermal [35, 36], electrospinning [37, 38], anodization [39-41], nanocarving [42, 43], and UV lithography with dry plasma etching [44] for the synthesis of 1D TiO_2 based nanostructures. Out of these, wet processing, such as hydrothermal, electrospinning and anodization requires multiple steps with appropriate control on processing variables. The resultant nanostructures are amorphous, which is a distinct disadvantage for many applications where crystallinity is required. Furthermore, wet processed TiO_2 nanostructures possess impurities. So, in many instances post-processing, such as purification and annealing are required. On the contrary, solid-state processing, such as UV lithography with dry plasma etching resulted in crystalline structures, but the equipment is too sophisticated, expensive and not easily scalable. Recently, a simple, inexpensive and highly scalable procedure has been developed for the synthesis of 1D TiO_2 based nanostructures on Ti [31, 45-51] and Ti alloy [25, 52, 53] substrates by thermal oxidation. This process

requires heating of Ti substrates at temperatures ranging from 600 °C to 850 °C in very low oxygen containing environment [31, 45-51]. This process has some distinct advantages over wet chemical and solid state processing. The most significant advantages are being low-cost and scalability for the large scale production [54]. Moreover, while most of the other fabrication processes produce homogeneous single phase nanostructures, the thermal oxidation process provides the opportunity to grow core-shell hetero-structures [25, 53]. The possibility of growing hetero-structures can be optimized by choosing proper alloying composition in the substrate [25, 53], or by employing an oxidizing environment other than oxygen [31].

The growth of 1D TiO_2 nanostructures on Ti substrate by thermal oxidation process requires minute amount of O_2 [51]. High concentration of O_2 resulted in oxide layer on Ti substrates instead of 1D nanostructures [46, 47]. On the other hand, minute amount of dry O_2 resulted in very low coverage of 1D TiO_2 nanostructures [46]. In the literature, different oxidation mediums, such as acetone (CH_3COCH_3) [31, 45-47], ethanol (C_2H_5OH) [47, 49, 50], acetaldehyde (CH_3CHO) [47] and dibutyltin dilaurate ($C_{32}H_{64}O_4Sn$) [48] in Ar were used for the growth of 1D TiO_2 nanostructures on Ti substrates. However, usage of acetone [31, 45-47], ethanol [47, 49, 50], acetaldehyde [47] and dibutyltin dilaurate [48] as oxidation medium is not cost effective and special gas flow system is required. The presence of carbon layer was observed on the 1D TiO_2 nanostructures, which requires post-annealing to be removed [31]. Beside this, potassium based catalyst, such as KOH [19, 55] and KF [56] were also investigated for the growth of 1D TiO_2 nanostructures on Ti by thermal oxidation process. Results showed that the originated 1D nanostructures are shorter with length up to 600 nm [19] and the nanostructure possessed potassium as doped element [55, 56]. In contrast, usage of commercial Ar containing ppm level of O_2 as impurity in the presence of humidity is an affordable oxidation medium of Ti for the growth of 1D nanostructures. The presence of humid Ar with ppm level of O_2 is relatively unexplored for the growth of 1D nanostructures on Ti substrates.

The presence of multi-layered oxides were observed beneath the 1D nanostructures during oxidation of metal oxides, such as Cu [57-59], Fe [60-62] and Ti-6Al-4V (Ti64) [25, 53]. Oxidation of these substrates resulted in the formation of CuO/Cu_2O [57-59], $Fe_2O_3/Fe_3O_4/FeO$ [60-62] and TiO_2-Al_2O_3/TiO_2 [53] layers on the surface of Cu, Fe and Ti64 substrates, respectively. Previously, it was proposed by Kumar *et al*. [57] that during oxidation of Cu substrate, stress is induced at the interface of CuO/Cu_2O layers due to difference in crystal structures, molar volume

and densities. During oxidation, the "induced stress" is released by creating new surfaces in the form of 1D CuO nanostructures. This stress-induced growth mechanism was also supported for the growth of 1D Fe_2O_3 [60-62] and core-shell TiO_2-Al_2O_3 [52, 53] nanostructures on Fe and Ti64 substrates, respectively. So far, no study has focused on the oxidation states of the oxide layer that forms beneath the 1D TiO_2 nanostructures during humid oxidation of Ti in oxygen deprived conditions. The oxide scale beneath the 1D TiO_2 nanostructures has not been investigated previously.

Besides the induced stress generated at the interfaces of oxide layers, the effects of "residual stress" imposed by ball milling [52], hammering [52], bending [63], sand blasting [59] and surface mechanical attrition treatment [64, 65] were investigated during oxidation for the growth of 1D nanostructures on Cu and Ti64 substrates. It was clearly demonstrated that residual stress imposed by these treatments significantly enhances the coverage and density of 1D nanostructures. Similar to induced stress, the residual stress also relaxes by forming new surfaces in the form of 1D nanostructures. So far, no study has been conducted to study the effect of residual stress on Ti substrates during oxidation for the growth of 1D TiO_2 nanostructures.

In this research work, a study was undertaken to synthesize 1D TiO_2nanostructurs by oxidizing Ti substrates in dry and humid Ar environment containing 5 ppm of O_2. Residual stress was imposed on the Ti substrates by ball milling and its effects on the growth of 1D nanostructures was investigated. The 1D nanostructures and oxide layers beneath the nanostructures was characterized by different techniques. Based on the results, a mechanism is proposed for the growth of 1D TiO_2 nanostructures.

2. Experimental Procedures

Ti particles (Powder Alloy Corporation, USA), Ti plates (Goodfellow Cambridge Limited, England) and Ti TEM grids (Ted Pella, 300 mesh) were investigated for the growth of one dimensional (1D) TiO_2 nanostructures by thermal oxidation. Prior oxidation, the Ti particles were stressed by ball milling. The residual stress in Ti particles was measured by XRD-$\sin^2\psi$ technique. Then the Ti particles were oxidized under optimum conditions to investigate the effects of residual stress on the growth of 1D nanostructures. The 1D nanostructures were characterized by different techniques to explain the growth mechanism.

2.1. Measurement of residual stress

To determine the effects of residual stress on 1D TiO_2 growth, the as-received Ti particles (Ti-0h) were milled in a planetary ball mill (Retsch: PM 400 - MA type) for 20 hr at 250 rpm in ambient environment. The milled Ti particles are designated as Ti-20h. Twenty four ZrO_2 balls having diameter of 1 cm and weight of 3 gm were used in the milling process. The weight ratio of ZrO_2 balls to Ti particles was 10:1.

The residual stress inside the Ti-0h and Ti-20h particles was measured using an X-ray diffractometer (XRD: PANalytical Empyrean) having Cu$K\alpha$ radiation (0.1540598 nm). The XRD-sin$^2\psi$ technique was employed to measure the residual stress by tilting the samples at different tilt angles (ψ) ranging from 0 to 40° [66-68]. The incident X-ray beam was introduced through a window to hit the sample surface at a fixed incident angle of Ω having a width, divergence slit and anti-scattering slit of 0.5 inch, 0.125° and 0.0625°, respectively. A computer controlled Omega-goniometer was used to tilt the samples. The as-received and titled Ti particles were scanned in the 2θ region from 136-142° for the (2 1 3) crystallographic plane at different ψ angles. The d spacing of the (2 1 3) crystallographic plane was calculated using the Bragg's law [69]. The residual stress inside the particles is calculated by the following equation [66-68].

$$\sigma = \frac{E}{1+\nu} \cdot m \qquad (1)$$

Where, σ is the residual stress, E is Young modulus, ν is Poison ratio and m is the slope of the d-sin$^2\psi$ curve. The average value of the elastic constant [E/(1+ υ)] for (2 1 3) crystallographic plane is reported to be 90.3 GPa for commercial Ti substrates [70]. So, for the measurement of residual stress of Ti substrates equation (1) can be re-written as follows:

$$\sigma = 90.3 \times m \qquad (2)$$

2.2. Thermal oxidation of Ti substrates

Prior oxidation, the Ti particles (Ti-0h and Ti-20h), Ti plates and Ti TEM girds were cleaned in 30 vol% HCl for 30 min followed by cleaning in distilled water. For oxidizing Ti-0h and Ti-20h particles, ethanol was taken in a small

bottle and 5 wt% of particles were dispersed in it. The suspensions were ultrasonicated for 1 h. About 10 µL of suspension was taken using micropipette and dropped on the alumina substrate. The Ti plates were cut having dimensions of 15 mm x 15 mm x 1 mm and the surface to be oxidized was polished until 0.02 µm finishes using standard metallographic techniques to incorporate stress and defects on the surface. For the oxidation of Ti TEM grid, it was placed vertically inside a shallow recess (~1 mm) cut into a piece of bulk Ti.

The Ti particles along with alumina substrates, polished Ti plates and Ti TEM gird inside a shallow recess were placed inside the quartz tube of a horizontal tube furnace (Lindberg Blue M, TF5503A-1). The details of the experimental setup are presented in Ref. [52, 53]. In short, the quartz tube was connected through mass flow controller (MFCs: Sierra, C100L-CM-NR-2-0V1-SV1-PV2-V1) with a cylinder containing commercial Ar with 5 ppm O_2 as impurity. A bubbler containing 150 ml deionized (DI) water was placed in between the MFC and quartz tube and connected with appropriate gas piping system to create humid environment inside the quartz tube during oxidation. The relative humidity (RH) inside the quartz tube was monitored using a dew point transmitter (EE31-PFTE, E+E Elektronic Corporation). The bubbler was removed during dry oxidation of Ti. Before ramping up the furnace, the quartz tube was purged for 30 min with 5 ppm O_2 in Ar to create homogeneous oxidizing environment inside the quartz tube. Then the furnace was heated to the oxidation temperatures (700 or 750 °C) at a rate of 30 °C/min. The oxidation was carried out for 4 h. The total flow rate of the gases was maintained at 150 or 500 sccm. The slight variations in experimental conditions are due to variations in substrates, which require little adjustment for optimum coverage of 1D nanostructures. The oxidation conditions for different substrates are tabulated in Table 1. After oxidation, the furnace was cooled down to room temperature by opening the furnace lid, but the gases continued to flow inside the quartz tube.

Table 1: Experimental conditions for the growth of 1D TiO_2 nanostructures on Ti substrates by thermal oxidation.

Sample identification	Oxidation environment	Oxygen concentration	Background gas	Total gas flow rate	Oxidation duration	Oxidation temperature
As-received Ti particles (Ti-0h)	Humid	5 ppm	Ar	150 sccm	4h	750 °C
	Dry			150 sccm		750 °C
Milled Ti particles (Ti-20h)	Humid			150 sccm		750 °C
Ti plate	Humid			500 sccm		750 °C
Ti TEM grid	Humid			500 sccm		700 °C

2.3. Characterization of oxidized Ti substrates

The materials were characterized at different stages using field emission scanning electron microscope (FESEM: FEI Quanta FEG 450) equipped with energy dispersive X-ray (EDX: Oxford instruments) spectroscope, transmission electron microscope (TEM: FEI, Model CM200), X-ray diffractometer (XRD: PANalytical Empyrean) and X-ray photoelectron spectroscope (XPS: ULVAC-PHI Quantera II). The particle size and morphological observations of 1D nanostructures were performed under FESEM. The average density of 1D nanostructures were calculated from the low magnification FESEM images by counting the number of nanostructures in per unit area. The compositional analysis was performed under EDX spectroscope. The crystal structure and growth direction of the nanostructures were determined using TEM equipped with selected area diffractometer (SAD). The phase analysis was performed using XRD with Cu$K\alpha$ radiation (0.1540598 nm). The oxidation states of Ti were investigated using XPS with monochromatic Al$K\alpha$ radiation (1486.6 eV). The instrument base pressure was $3x10^{-7}$ Pa and operated at 25.6 W. The diameter of the beam was 100 µm. Electron flood gun and mono-atomic Ar ion gun was used as charge neutralizer. The wide scan analysis was performed using pass energy of 280 eV with 1eV per step. The narrow scan (chemical states analysis) was performed using pass energy of 112 eV with 0.1 eV per step. The Multipak Spectrum: ESCA software was used for the analysis the XPS data.

3. Results and Discussion

The first approach of this study was to characterize the Ti substrates and investigate the effects of residual stress on the growth of one dimensional (1D) TiO_2 nanostructures during oxidation. The as-grown nanostructures together with the oxide scale formed on Ti substrates were characterized by different techniques, such as field emission scanning electron microscope (FESEM), energy dispersive X-ray (EDX) spectroscope, transmission scanning microscope (TEM), X-ray diffractometer (XRD) and X-ray photoelectron spectroscope (XPS). Based on the findings a mechanism is proposed to explain the growth of 1D TiO_2 nanostructures on Ti substrates during thermal oxidation.

3.1. Characterizations of as-received and milled Ti particles

Figure 1(a) shows the FESEM image of the as-received Ti particles (Ti-0h). The as-received Ti particles have irregular shape with an average size of 70 µm. The EDX spectroscope spot analysis of Ti particles shows Ti, C and

O peaks (Figure 1(b)). The C peak is obtained from surface contaminants or conductive carbon tape which was used to stick the particles with FESEM sample holder. The O peak originates from surface oxides of Ti particles. The XRD peaks of as-received Ti particles are shown in Figure 1(c).Peaks from α-Ti (hexagonal) phase are seen in the XRD pattern. No peak from β-Ti(body centered cubic) is seen in the XRD analysis. In addition, no peak belonging to the oxides of Ti or any other contaminants is observed. So, the O peak observed in EDX spectroscope analysis (Figure 1(b)) is obtained from surface oxides and it is expected that the thickness of the surface oxide layer is very small.

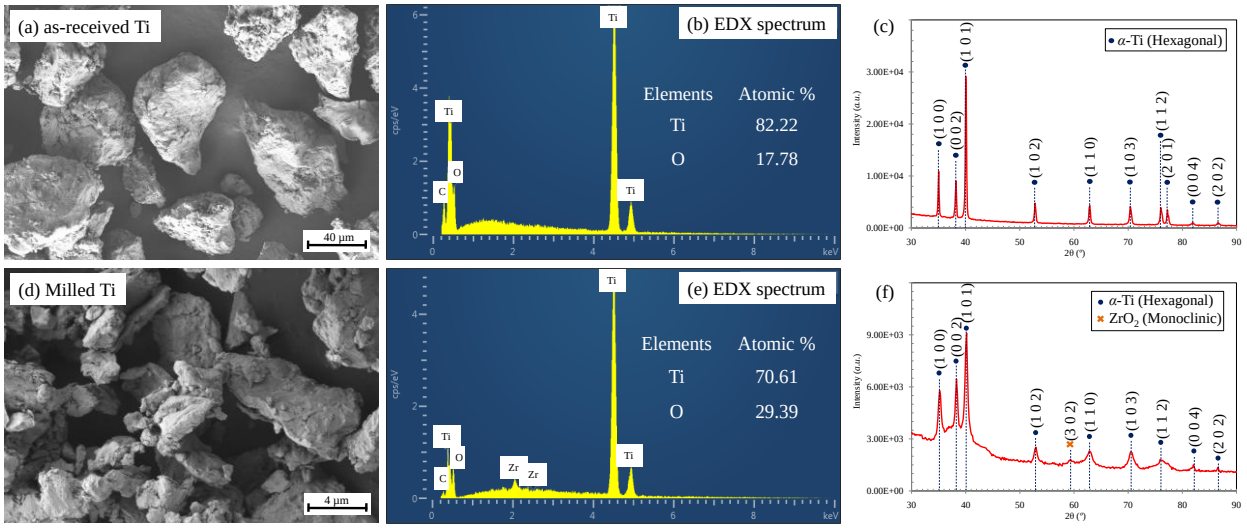

Figure 1: (a-c) FESEM image, EDX spectrum (spot analysis), and XRD peaks of as-received Ti particles, respectively and (d-f) FESEM image, EDX spectrum (spot analysis), and XRD peaks of the milled Ti particles, respectively.

The Ti particles were ball milled for 20 h at 250 rpm in a planetary ball mill and designated as Ti-20h particles. Figure1(d) shows the FESEM image of Ti-20h particles. After milling, the particles have irregular shape with size ranging from 3 to 10 µm. Peaks of Ti, Zr, C and O are seen in the EDX spectrum of Ti-20h particles (Figure 1(e)). The Zr peaks were obtained from the erosion of ZrO_2 balls, which were used to mill Ti particles. Such ZrO_2 contaminations were also observed by other researchers during long hours of milling [71]. As mentioned earlier, the C peak is obtained from contaminants or conductive carbon tape. On the other hands, O peak is obtained from surface oxides either from TiO_2 or ZrO_2. The XRD peaks of milled Ti particles are shown in Figure 1(f). The α-Ti (hexagonal) phase is observed in the XRD analysis of milled Ti particles. No TiO_2 peak is seen in the XRD.

However, a small ZrO_2 peak appeared at 2θ angle of 59.6°. So, it can be concluded that milling do not alter the phase of Ti particles but the particle size is significantly reduced.

3.2. Effects of residual stress on 1D growth

Residual stress was incorporated inside the Ti particles during ball milling. The XRD-$\sin^2\psi$ technique was used to evaluate the residual stress in Ti-0h and Ti-20h particles [66-68]. According to Zheng [72] and Luo *et al*. [73], the diffraction peaks occurring at Bragg angles of 130° or higher should be chosen for measuring residual stress. For this reason, the Ti-0h and Ti-20h particles were scanned at 2θ angles from 136° to 142° targeting the peak from (2 1 3) crystallographic planes of α-Ti, which generally appears at 139.5° when Cu$K\alpha$ radiation is used. It was also recommended by Prevéy *et al*. [70] to scan the (2 1 3) crystallographic plane of Ti to measure the residual stress.

The particles were scanned at different tilt angles (ψ) ranging from 0° to 40° as shown in Figure 2(a-b). To obtain good accuracy, the particles were scanned for eight times at each tilt angles and plots are superimposed in Figure 2(a-b). In general, the (2 1 3) peaks are shifted at different tilt angles. The shifts are more evident for Ti-20h compared to Ti-0h particles. The peaks become shorter and wider in Ti-20h particles. Broadening of peaks is an evidence of stress accumulation in Ti-20h particles.

The lattice spacing (d) corresponding to the peaks of (2 1 3) crystallographic planes for all eight scans are calculated using the Bragg's law and average lattice spacing (d) is plotted against $\sin^2\psi$ in Figure 2(c) for both Ti-0h and Ti-20h particles. The slopes (m) of the d-$\sin^2\psi$ plot were found to be +0.001 and +0.003 for Ti-0h and Ti-20h particles, respectively. Substituting these values in equation (2), the residual stresses are found to be +90.3 MPa (compressive) and +270.9 MPa (compressive) for Ti-0h and Ti-20h particles, respectively as shown in Figure 2(d). Though the residual stress is calculated using eight scans but Figure 2(d) does not have standard deviation as the average value of m from eight sets of data is used for the calculations.

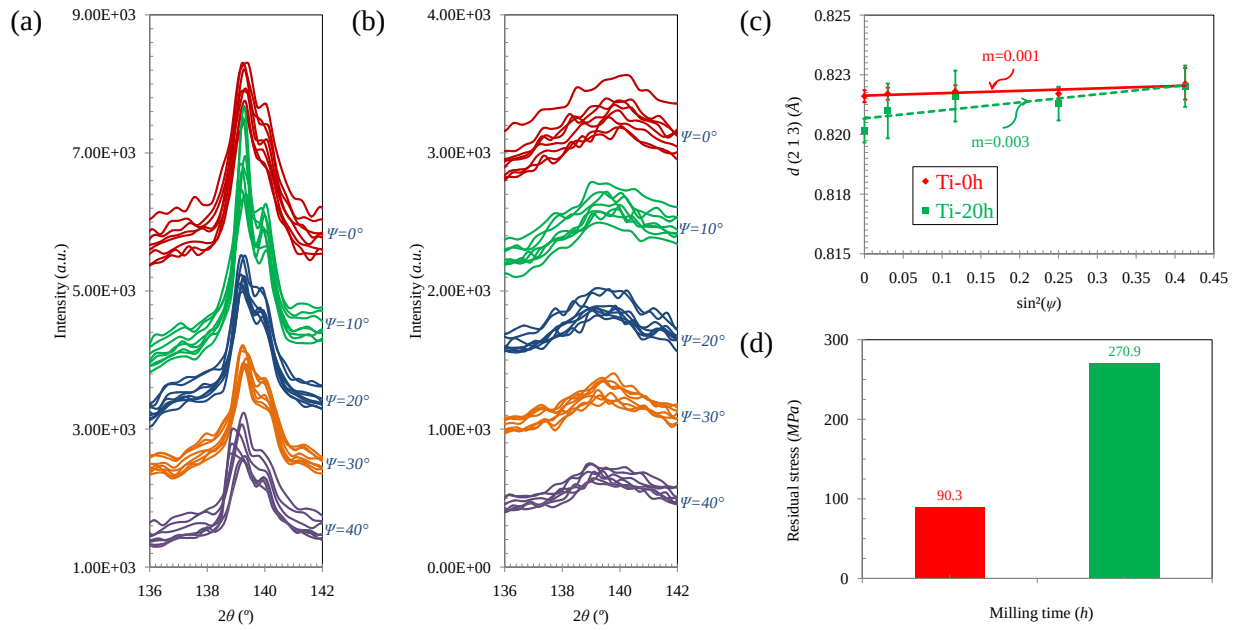

Figure 2: (a-b) XRD peaks of (2 1 3) crystallographic planes in Ti-0h and Ti-20h particles at different tilt angles (ψ). The particles were scanned for eight times at each tilt angles and the plots are superimposed. (c) d-sin$^2\psi$ plot for the Ti-0h and Ti-20h particles, and (d) estimated residual stress in Ti-0h and Ti-20h particles.

According to literature, there are some sources of error in the XRD-sin$^2\psi$ technique for determining residual stress. These include the errors in measurement of diffraction peaks, nonlinear relation between lattice spacing (d) and sin$^2\psi$ due to the grain interactions, anisotropic elastic property of crystalline materials and instrumental conditions [72, 73]. Nonetheless, the estimated values show the accumulation of higher amount of compressive stress in milledTi-20h particles. The XRD analysis shown in Figure 1(f) also indicates the accumulation of stress in Ti-20h particles through peak broadening when compared with the XRD of Ti-0h particles shown in Figure 1(c). It should be noted that the values of residual stress may not be accurate, but the values are suggestive that the accumulated residual stress is three times higher in the milled particles compared to as-received Ti particles.

To elucidate the effects of residual stress imposed by ball milling, the Ti-0h and Ti-20h particles were thermally oxidized for 4 h at 750 °C in the presence of 5 ppm O_2 in humid Ar environment flown at a rate of 150 sccm. The FESEM images of Ti-0h and Ti-20 particles after humid oxidation are shown in Figure 3. Higher coverage of 1D nanostructures is observed on the surface of Ti-20h particles compared with Ti-0h. Moreover, in Ti-0h particles the

1D nanostructures preferentially grow at the corner or bent regions, where higher amount of residual stress is present. The bulk surface of Ti-0h particles consists of oxide scale or very low coverage of 1D nanostructures (Figure 3(a)). On the other hand, the surface of Ti-20h particles is fully covered by 1D nanostructures (Figure 3(b)). The average density of 1D nanostructures in Ti-0h and Ti-20h particles is are 1.27×10^{10} m^{-2} and 2.7×10^{11} m^{-2}, respectively. The number of 1D nanostructures increases ~21 times in the milled particles. It should be noted that the general distribution of the 1D nanostructures is more or less the same for certain condition of oxidation. However, the values of average density are not absolute but suggestive that residual stress significantly enhances the coverage of 1D nanostructures.

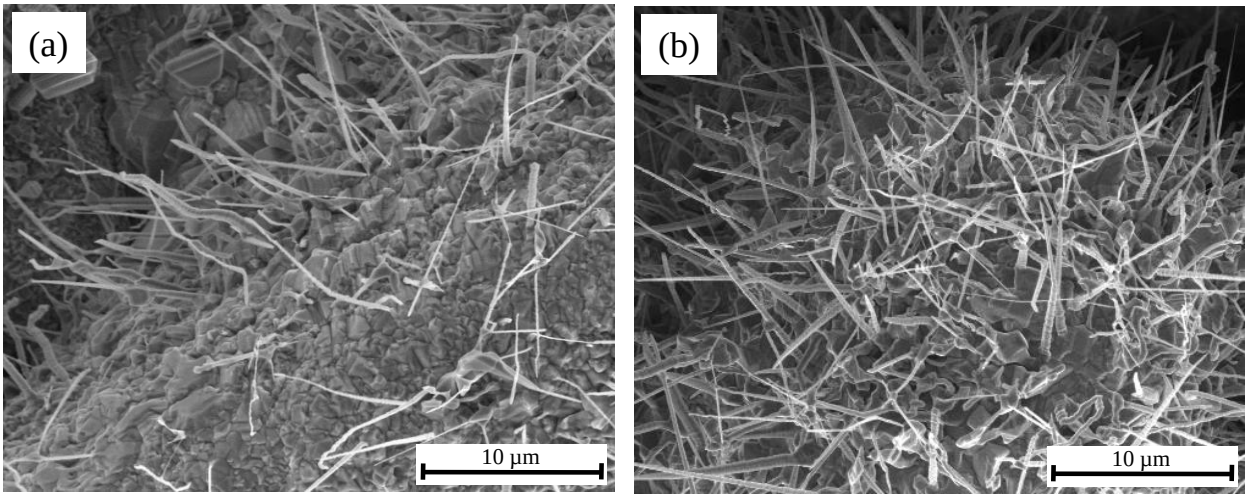

Figure 3: FESEM images of Ti-0h and Ti-20h particles after oxidation for 4 h at 750 °C in humid Ar containing 5 ppm of O_2 flown at a rate of 150 sccm.

Previously, the effects of residual stress on the growth of 1D nanostructures during thermal oxidation of Ti-6Al-4V (Ti64) particles and plates were investigated and similar results were found [52, 53]. It was observed that residual stress imposed by ball milling of Ti64 particles or hammering of Ti64 plates significantly enhanced the density of 1D nanostructures during thermal oxidation. Similar phenomena were also observed for the growth of CuO nanowires on Cu substrates by thermal oxidation. It was reported that residual stress imposed on Cu substrates by bending [63], sand blasting [59] and surface mechanical attrition treatment [64, 65] significantly enhances the coverage of CuO nanowires during thermal oxidation. It is believed that the imposed residual stress is released during humid oxidation of Ti substrate by creating new surfaces in the form of 1-D nanostructures [52, 57]. The

mechanism of the growth of 1D nanostructures and the role of stress on Ti substrates during oxidation is discussed separately in Section 3.4.

3.3. Characterizations of oxidized Ti substrates

The 1D nanostructures grown on Ti particles during thermal oxidation are not straight and bend to certain angles. Four types of 1D morphologies namely (a) stacked, (b) ribbon, (c) plateau and (d) lamp-post shaped nanostructures are seen during oxidation of Ti substrates as shown in Figure 4. These types of 1D nanostructures are randomly distributed on the surface oxidized under similar condition. However, the prevalence of stacked morphology is most frequently observed. Stacked morphology appears to be composed of nano-crystal platelets grown over one another along the length of 1D nanostructures as shown in Figure 4(a). However, the dark field (DF) TEM image of small portion of stacked nanostructures confirms the single crystal nature (inset of Figure 4(a)). The contrast observed in stacked nanostructures is most likely due to thickness variations. The length of the stacked nanostructures is typically 5 to 10 μm. The nanostructures have non-uniform thickness varying from 50-500 nm. Generally, the thickness of the nanostructure is wider at the root compared to the top. The entanglement behavior is most commonly seen in stacked nanostructure. Beside this, formation of nodes is seen on these nanostructures as shown in Figure 4(a), where two 1D nanostructures are originated from the node. It is assumed that defect sites are involved for the bending of stacked nanostructures. Further studies are required to obtain a better understanding of the root causes of bending and formation of nodes.

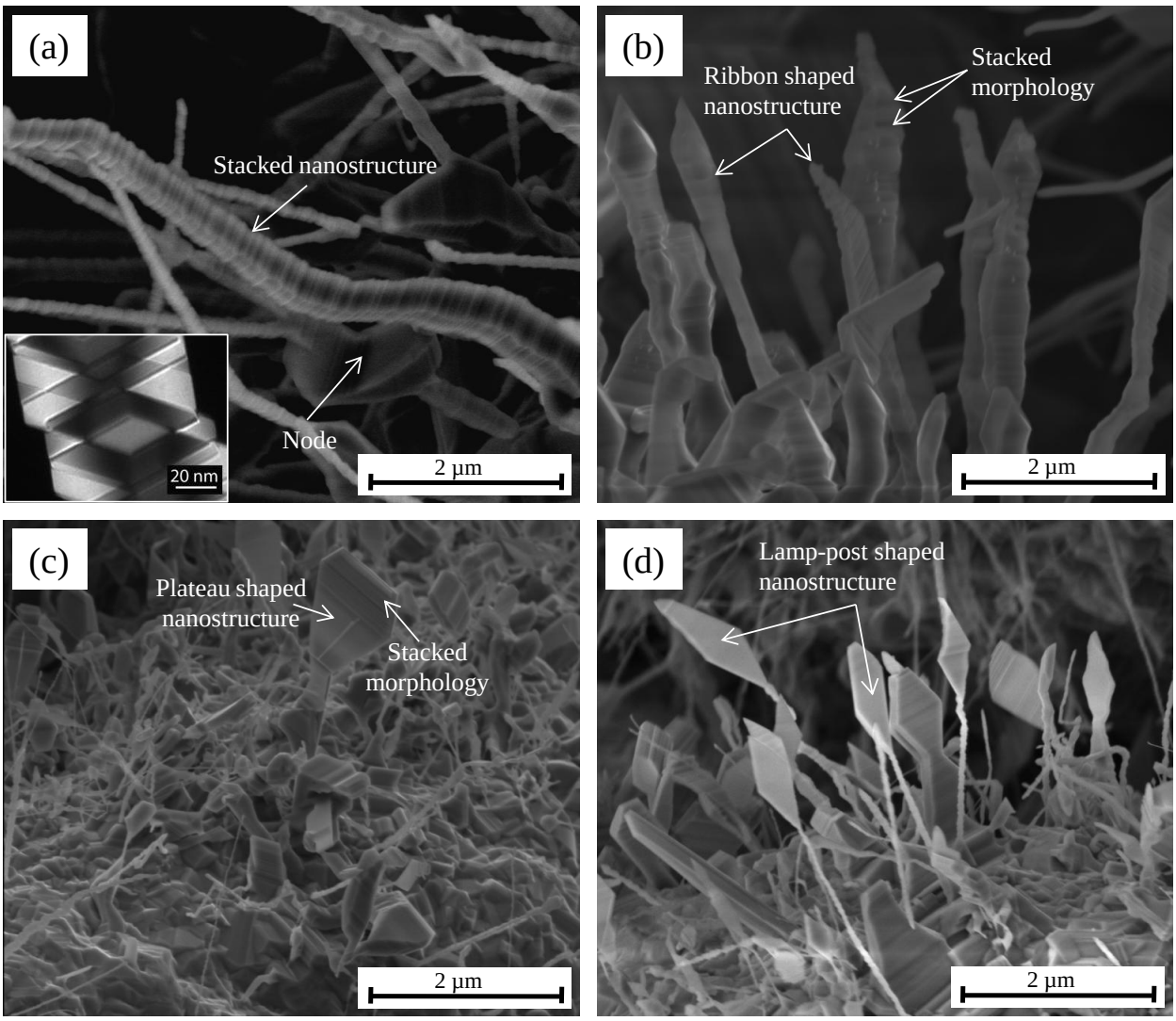

Figure 4: The growth of different types of 1D morphologies during oxidation of Ti particles (a) stacked nanostructure and inset showing DF TEM image of stacked nanostructure, (b) ribbon shaped nanostructure, (c) plateau shaped nanostructure, and (d) lamp-post shaped nanostructure.

The ribbon shaped nanostructures are the second most widely observed morphology during thermal oxidation of Ti substrates. The ribbons have flat shape at the root but tapered at the top as shown in Figure 4(b). Some stacked type morphology and entanglement is also evident in ribbon shaped nanostructures. The ribbons are 2-4 µm long with width and thickness of 300-400 nm and 60-80 nm, respectively. Plateau shaped morphology is observed at discrete locations during oxidation of Ti substrates. One plateau shaped nanostructure is shown in Figure 4(c). Plateau morphology appears in different size and shapes and has non-uniform width. Typically, plateau shaped

nanostructures are 2-4 µm long with a thickness of 60-80 nm. The width of the nanostructure can be as high as 2 µm at some points. Stacked morphology and entanglement is also evident on plateau nanostructures. The lamp-post shaped nanostructures are also seen during oxidation of Ti substrates as shown in Figure 4(d). However, the frequency of appearance of lamp-post shaped nanostructures is quite low. Lamp-post shaped nanostructures are combinations of two morphologies: (1) stacked morphology at the root and (2) a rhombus shaped morphology at the top. Typically, these nanostructures are 6-8 µm long. The diagonals of the rhombus in lateral and longitudinal directions are 0.8-1 µm and 1.6-2 µm, respectively. Evidence of stacked morphology and entanglement are also observed in lamp-post shaped nanostructures. Though four different morphologies are observed during oxidation of Ti particles, some features, such as stacking and bending are common. Moreover, the stacked morphology occupies roughly 80% of total as-grown 1D nanostructures. Based on the current investigation it is impossible to say anything conclusive about the reason why the growth of one type of nanostructure is predominating over the others. The variances in morphologies may be due to variations in surface conditions, such as stress, defects, impurities, grain size, etc. Further analysis is necessary to determine what conditions favor the growth of one type of nanostructure over the other.

To understand the crystal structure and growth direction of nanostructures, Ti TEM grid was thermally oxidized for 4 h at 700 °C in humid Ar environment containing 5 ppm O_2 flowing at a rate of 500 sccm. The reason for growing 1D nanostructures on Ti grid rather than Ti particles is to simplify the observation process of the nanostructures under TEM. In general, it is hard to detach 1D nanostructures from the particles by ultrasonication for the observation under TEM as performed in a previous study [74]. The particles may break during ultrasonication and may be contaminated with the oxide scales formed beneath the 1D nanostructures. On the other hand, the Ti grids can be directly used for high resolution observation under TEM without any further processing after oxidation. The FESEM image of the oxidized Ti grid is shown in Figure 5(a), where a large number of 1D nanostructures is seen growing radially into the grid holes. It should be noted that the number of defect sites, active sites and edges can be different in Ti grid compared with the milled particles. But, close observation to the oxidized Ti grid shows that the 1D nanostructures preferentially grow at the edges compared to the interior. The interior of the grid has higher thickness and the edges of the grid is probably stressed. This finding is aligned with Figure 3(a), where the nanowires grow only at the corner or bent regions of Ti-0h particles. As similar scenario is observed both on Ti

particles and grid with similar morphological variations under similar experimental conditions, it can be concluded that the growth direction of 1D nanostructures on Ti particles and grid is comparable.

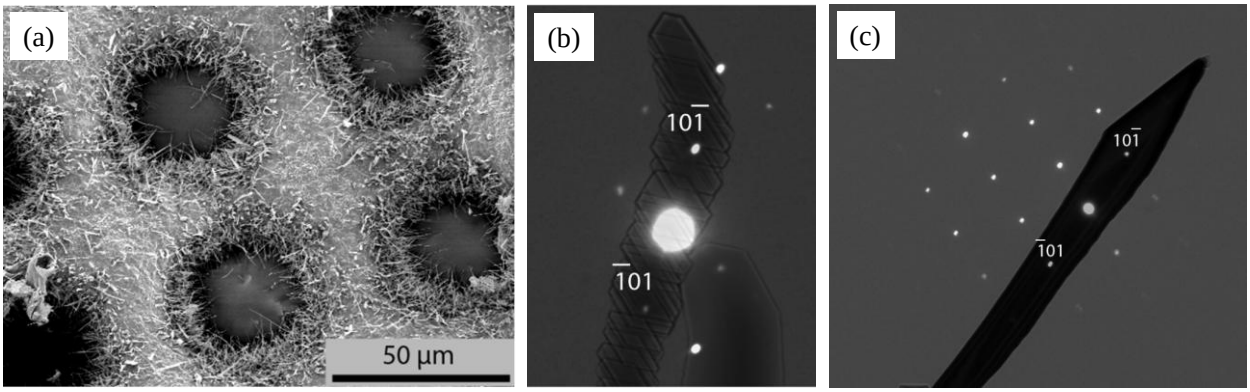

Figure5: (a) FESEM image of Ti TEM grid oxidized at 700 °C for 4 h in humid Ar containing 5 ppm O_2 flowing at a rate of 500 sccm, (b) BF TEM image of stacked nanowires superimposed with corresponding diffraction pattern, and (c) BF TEM image of ribbon shaped nanowires superimposed with corresponding diffraction pattern.

Figure 5(b) shows bright field (BF) TEM image of stacked nanostructures and the corresponding selected area diffraction (SAD) pattern is superimposed on it. The TEM gird was tilted to obtain strong diffraction pattern, which was not exactly on the zone. However, it is still possible to index the pattern to a [1 1 1] type zone axis of tetragonal rutile TiO_2. The growth direction of the nanostructures is <1 0 1>. Figure 5(c) shows BF TEM image of ribbon-shaped nanostructure superimposed with SAD pattern. The bright and dark contrast appears on the nanostructure are indicative of thickness variations. The SAD pattern appears to be tetragonal rutile TiO_2 with [1 1 1] zone axis. The ribbon shaped nanostructure grows along <1 0 1> directions, which is similar to the stacked morphology. So, from TEM analysis it is confirmed that the 1D nanostructures composed of rutile TiO_2 having <1 0 1> growth directions.

The growth direction of TiO_2 nanostructures found in the present case is different from other researchers. Previously, Peng *et al*. [46-48] and Daothong *et al*. [50] reported that 1D TiO_2 nanostructures grows along <0 0 1> direction. However, they oxidized Ti substrates in different mediums, such as acetone [46, 47], ethanol [50] or dibutyltin dilaurate [48] in Ar as tabulated in Table 2. In the present case, humid Ar containing 5 ppm O_2 is used for oxidizing Ti substrates and the growth direction is found to be <1 0 1>. So, a different mechanism is predicted for the growth of 1D TiO_2 nanostructures on Ti substrates during humid oxidation which is discussed in Section 3.4.

During oxidation of Ti substrates, the 1D TiO_2 nanostructures are originated from the oxidized surface. To investigate the elemental composition of oxidized surface, EDX spectroscopy and XRD analysis was performed. Figure 6(a) shows a typical EDX spectrum of Ti-20h particles after oxidizing at 750 °C for 4 h with 5 ppm of O_2 in humid Ar at a flow rate of 150 sccm. The inset of the figure is showing the corresponding oxidized Ti-20h particle. The presence of Ti and O peaks are seen in the EDX spectrum with small amount of C peak. The C peak is obtained from the carbon tape used for sticking the sample on FESEM sample holder or contaminations. Spot analysis at different locations of the oxidized particles shows 35.5 at% of Ti and 64.5 at% of oxygen, which is very close to the atomic ratio of Ti and O in TiO_2. The EDX analysis confirms that the top of the oxidized surface is TiO_2.

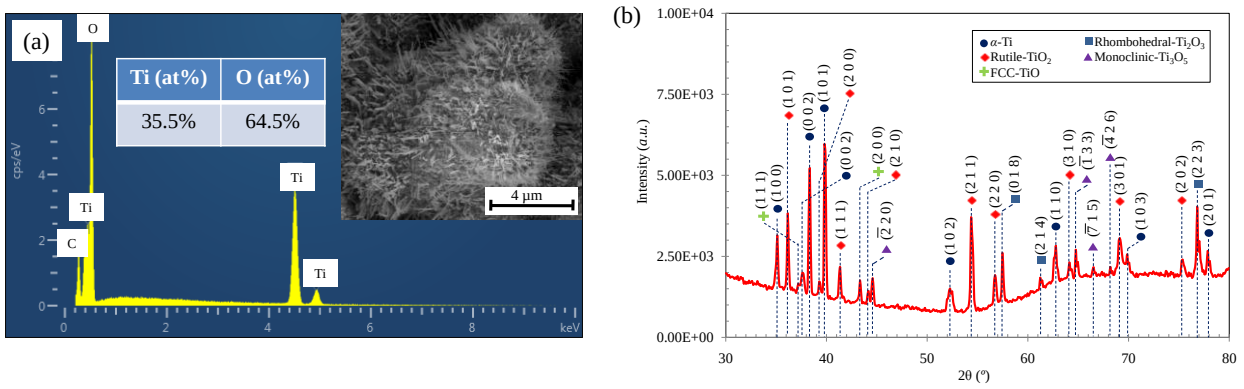

Figure 6: (a) EDX spectrum on oxidized Ti-20h particles and the inset showing the oxidized Ti-20h particle, and (b) XRD peaks of Ti-20h particles oxidized for 4 h at 750 °C containing 5 ppm of O_2 in humid Ar at a flow rate of 150 sccm.

Figure 6(b) shows the XRD peaks of Ti-20h particles oxidized under similar conditions. The presence of tetragonal rutile TiO_2 is evident in the XRD peaks. However, some lower valence oxides, such as monoclinic Ti_3O_5, rhombohedral Ti_2O_3 and face centered cubic TiO are also seen in the XRD peaks. In the literature, it was reported that lower valence oxides are formed during humid oxidation of Ti [75-77]. The lower valence oxides forms multiple layers at the oxide-metal interface and TiO_2 forms at the gas-oxide interface [75-77]. In the present case, similar scenario is anticipated though the experimental conditions were oxygen deprived. In XRD, some α-Ti peaks are observed, which comes from the un-oxidized core of Ti particles.

To further confirm different oxidation states, Ti plates were oxidized for 4 h at 750 °C in humid Ar containing 5 ppm O_2 flown at a rate of 500 sccm and analyzed under XPS. To incorporate stress and defect sites similar to the milled Ti particles, prior oxidation the Ti plates were polished using standard metallographic techniques until 0.02 µm finishes. Figure 7 shows the XPS spectra of oxidized Ti plate. The Ti*2p* peaks (Ti$2p_{3/2}$ and Ti$2p_{1/2}$) are seen at binding energies of 456.8 and 462.01 eV, respectively (Figure 7(a)). The Ti*2p* profile is deconvoluted into three Ti*2p* components (dotted lines) with binding energies of 454.2, 456.8 and 461.5, which represents the oxidation states of Ti^{2+}, Ti^{3+} and Ti^{4+} oxides, respectively (Figure 7(b)). Layering of lower valence oxides underneath TiO_2 layer are reported in the literature [75-77]. But, XPS should not be able to detect lower oxidation states of Ti if they are layered below the TiO_2. The possible reason for the existence of the peaks of lower oxidation state of Ti in XPS spectra could be due to peeled-off oxide layer during XPS observation. To understand this issue, the samples were cross-sectioned and observed under FESEM equipped with EDX (Figure 8). Beside this, the obtained values of binding energies of the deconvoluted Ti*2p* peaks is slightly deviate from the literature, which occurred at 455.34, 457.13 and 458.66 eV for Ti^{2+}, Ti^{3+} and Ti^{4+} oxides, respectively [78]. No peaks belonging to Ti_3O_5 is observed in the XPS spectra though it is observed in XRD peaks (Figure 6(b)).

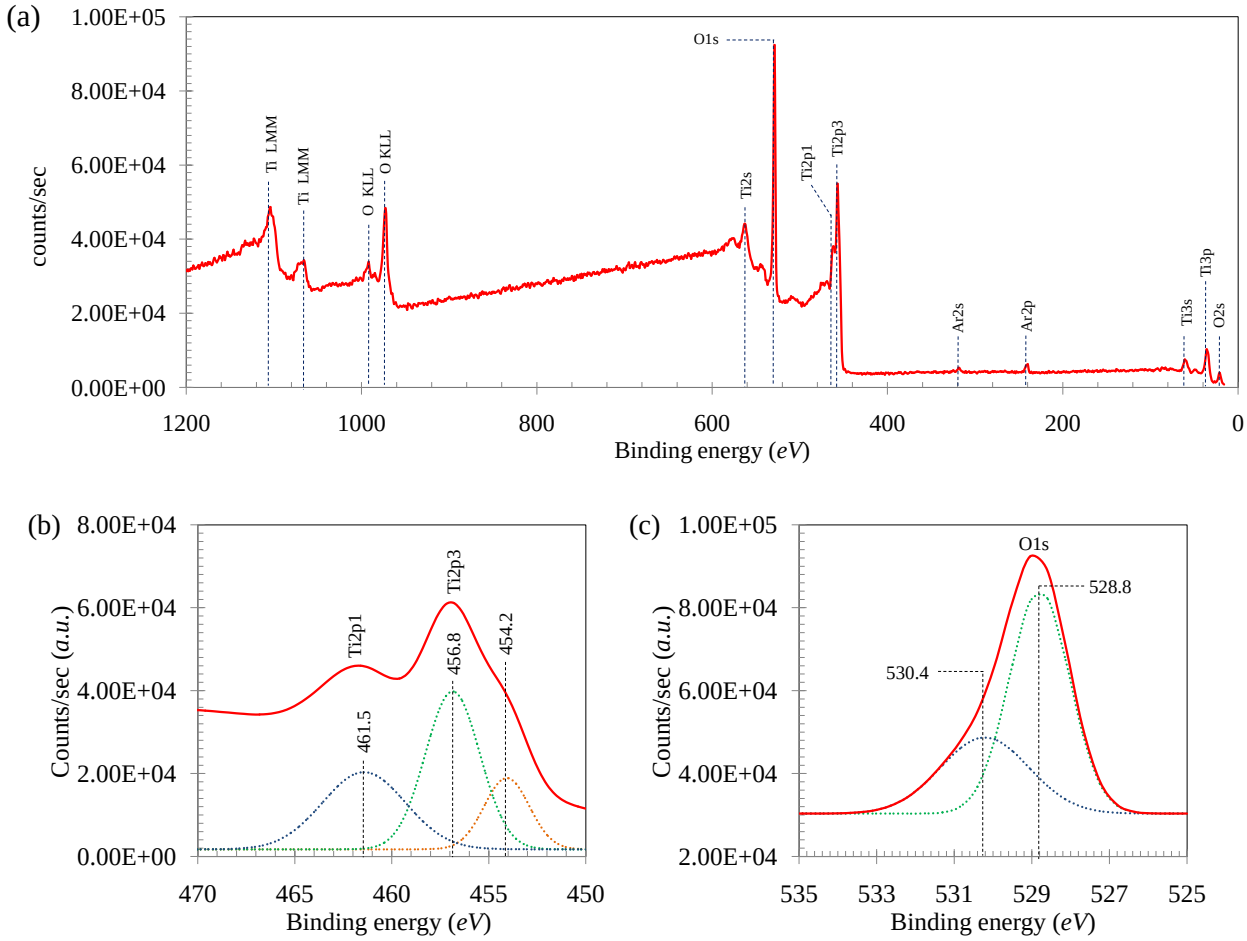

Figure 7: (a) XPS spectra of Ti plate oxidized at 750 °C for 4 h in the presence of 5 ppm O_2 in humid Ar, (b) narrow scan of Ti*2p* spectra, and (c) narrow scan of O1s spectra. The dotted lines in Figure (a) and (b) represent the deconvoluted Ti*2p* and O*1s* profile, respectively.

The occurrence of O*1s* peak is observed at the binding energy of 529.05 eV as shown in Figure 7(a). The O*1s* profile is deconvoluted into two components (dotted lines) having binding energies of 530.4 and 528.8 eV as shown in Figure 7(c). The major O*1s* peak at 528.6 eV is associated with TiO_2 or Ti_2O_3 [75]. In the literature, the O*1s* binding energy for TiO_2 is reported to be 529.9 eV [79]. The minor O*1s* peak at 530.4 eV is assigned to hydroxyl species on the Ti surface. In the literature, this minor peak is reported at 531.86 eV for hydroxyl species on the surface [80]. So, it is likely that during humid oxidation of Ti, hydroxyl species is adsorbed on the surface of Ti.

To further elucidate the presence of lower valence oxides, Ti particles were mounted in epoxy after oxidizing for 4 h at 750 °C in humid Ar containing 5 ppm of O_2 having total flow rate of 150 sccm. The particles were polished and observed under FESEM in cross-section as shown in Figure 8. It is seen that oxide layer(s) forms beneath the 1D nanostructures after oxidation. The total thickness of the oxide layers(s) is ~10 µm after 4 h of oxidation. The layering of lower valence oxides is not clearly resolved under FESEM and for this reason EDX spectroscope was carried out at different depth of the oxide layer(s). It should be noted that the spatial resolution of EDX spectroscope is in micron range and to overcome this problem at least 10 spots were analyzed to calculate the average atomic percentage of Ti and O. The average atomic ratio of O to Ti (O:Ti) is calculated from the results and presented in Figure 8. Results reveal that the atomic ratio of O:Ti varies from 2.2±0.82 to 2±0.14 from the top surface (point *A*) to a depth of ~6.5 µm (point *C*), respectively. These atomic ratios are very close to the O:Ti ratio in TiO_2. Some sort of cracks are observed beneath point *C* and assumed to have different compositions. The atomic ratio of O:Ti beneath the cracks (point *D*) is 1.6±0.27, which is close to the atomic ratio of O:Ti in Ti_3O_5. Finally, near to the metal/oxide interfaces (point *E*), the atomic ratio of O:Ti is about 1±0.03, which is basically TiO. Though the EDX analysis is not exact but the results are indicative of the formation of different oxide layers during humid oxidation of Ti. The outermost layer is TiO_2. Beneath TiO_2, the presence of Ti_3O_5 and TiO is resolved under EDX spectroscope. However, the presence of Ti_2O_3 is not observed in EDX analysis but present in the XRD peaks (Figure 6(b)) and XPS spectra (Figure 7). So, it is concluded that the formation of TiO_2 and lower valence of oxides are evident during humid oxidation of Ti in oxygen deprived condition as observed by XRD (Figure 6(b)), XPS (Figure 7) and FESEM equipped with EDX spectroscope (Figure 8).

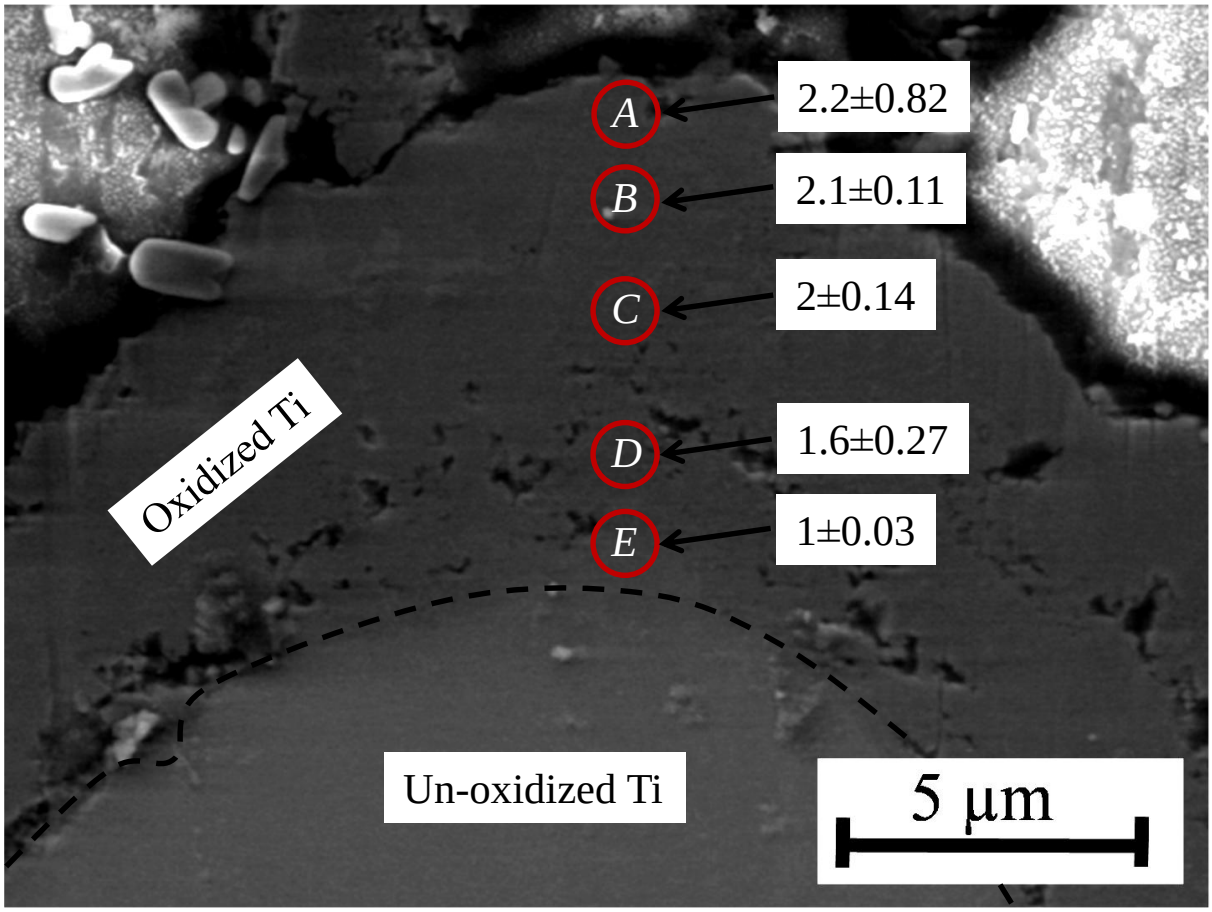

Figure 8: Cross-sectional view of Ti particles oxidized for 4 h at 750 °C in humid Ar containing 5 ppm of O_2 having total flow rate of 150 sccm and showing the atomic ratios of O:Ti at different depth of oxide layers.

3.4. Mechanism of 1D growth

The relative humidity (RH) inside the quartz tube was measured using dew point transmitter. It reveals that the RH decreases slightly with increasing gas flow rate. With increasing the flow rate from 150 sccm to 500 sccm, the RH was increased from 93% to 96%, respectively. To understand the role of humid environment, Ti particles were oxidized under similar conditions except humidity. Figure 9(a) shows low magnification FESEM image of Ti-0h particles after oxidizing for 4 h at 750 °C in dry Ar containing 5 ppm O_2. In dry oxidation, oxide scale is seen with very low density of short 1D nanostructures at discrete locations (shown as *X*, *Y* and *Z*)on the surface of Ti-0h particles. High magnification FESEM image of locations *X*, *Y* and *Z* is shown in Figure 9(b-d). It is seen that 1D nanostructures having length of 1-2 µm grow at discrete locations of the surface of Ti-0h particles oxidized in dry

conditions. Similar low coverage of 1D TiO_2 were obtained by Peng *et al*. [46] during dry oxidation of Ti in 1 sccm O_2 flow in 200 sccm flow of Ar. Besides this, oxidation with high concentration of O_2 (99%) resulted in polycrystalline TiO_2 film [46, 47]. In the literature, high coverage of 1D TiO_2 nanostructures on Ti substrates was found during oxidation in environments containing acetone (CH_3COCH_3) [31, 45-47], ethanol (C_2H_5OH) [47, 49, 50], acetaldehyde (CH_3CHO) [47] and dibutyltin dilaurate ($C_{32}H_{64}O_4Sn$) [48] in Ar as tabulated in Table 2. So, it is clear that dry oxidation environment is not beneficial for the growth of 1D TiO_2 nanostructures. It is anticipated that the oxidation kinetics of Ti substrate is different in dry and humid environment. So far, no study reports the mechanism of the growth of 1D TiO_2 nanostructures on Ti substrates during humid oxidation in oxygen deprived conditions.

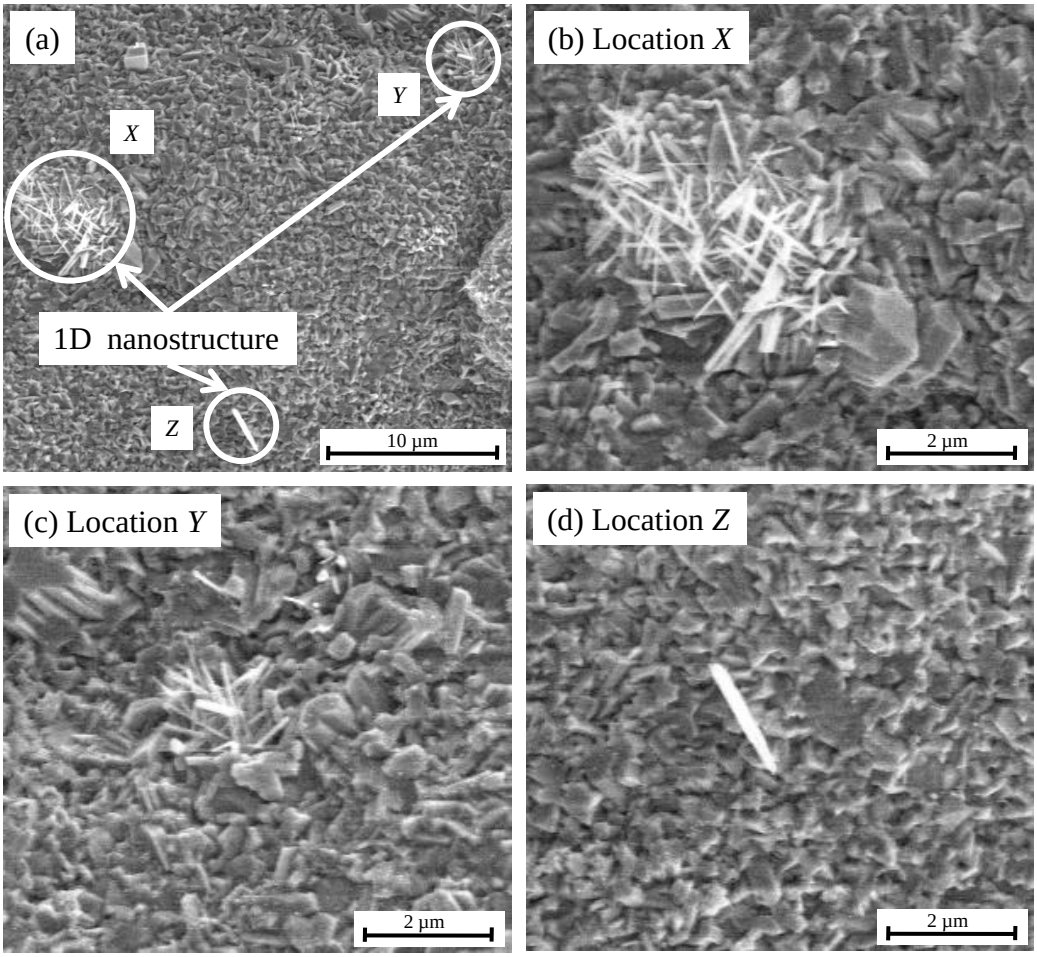

Figure 9: (a) Low magnification FESEM image of Ti-0h particles oxidized for 4 h at 750 °C in dry Ar containing 5 ppm O_2, and (b-d) high magnification FESEM image of locations having 1D TiO_2 nanostructures shown by circles in Figure (a).

The general oxidation behavior of Ti in humid air was studied by different researchers [76, 77, 81, 82]. During humid oxidation, water (H_2O) molecules dissociate to hydroxide ions (OH^-) and adsorb on the surface of Ti [76, 81, 82]. The Ti^{4+} ions diffuse interstitially to the surface and reacts with the surface adsorbed OH^- to form TiO_2 [76]. Hydrogen evolves as a byproduct by the following reactions [76].

$$H_2O \rightarrow H^+ + OH^-$$

$$Ti^{4+} + 2OH^- \rightarrow TiO_2 + 2H^+ + 2e^-$$

$$2H^+ + 2e^- \rightarrow H_2\uparrow$$

In addition, oxygen ions (O^-) diffuse inward via grain boundaries and reacts with Ti ions (Ti^{x+}, where value of x varies from 2 to 4) [81, 82]. Lower valence oxides of Ti, such as Ti_3O_5, Ti_2O_3, TiO are layered beneath the TiO_2 scale [77, 81]. In the present case, TiO_2 layer forms at the outermost oxide scale as seen from the EDX spectroscope analysis (Figure 6 and 8). The existence of lower valence oxides is observed from XRD (Figure 6(b)), XPS (Figure 7) and EDX (Figure 8) investigations. XPS result confirms that OH^- ion is adsorbed on the surface of Ti during humid oxidation (Figure 7(c)). Based on these findings, the mechanism for growth of 1D TiO_2 nanostructures on Ti substrate is proposed during humid oxidation and schematically presented in Figure 10.

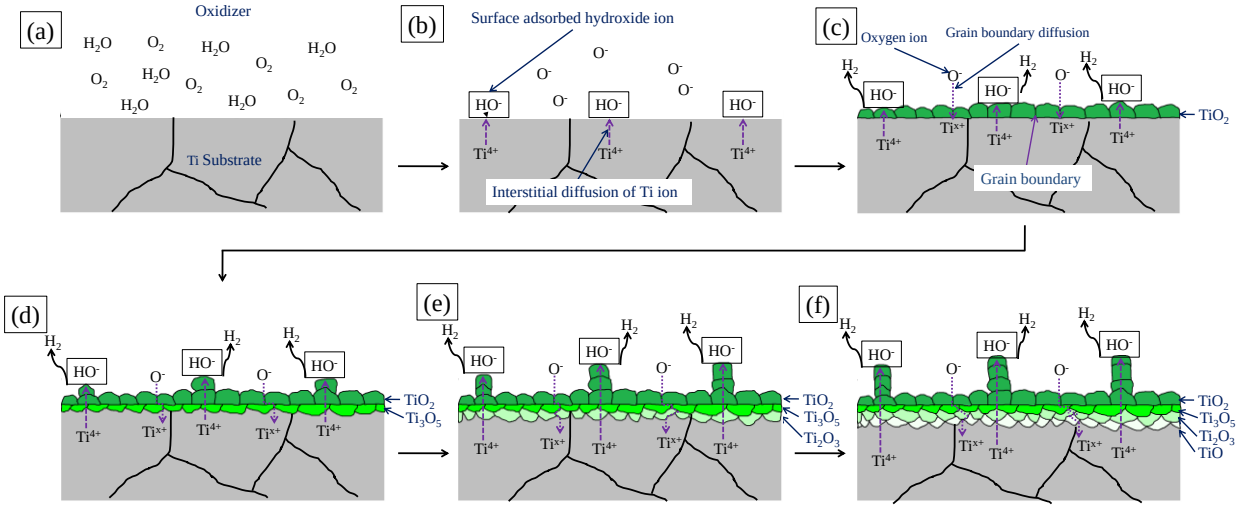

Figure 10: Flow-chart of the schematics mechanism of 1D TiO_2 nanostructure growth on Ti substrate during humid oxidation in oxygen deprived conditions.

Figure 10(a) shows a substrate containing α-Ti grains. During humid oxidation, H_2O molecules dissociate and OH^- ions adsorb on the surface of α-Ti grains as shown in Figure 10(b) [81-83]. The Ti^{4+} ions diffuse interstitially to the surface and reacts with surface adsorbed OH^- ions to form TiO_2 nuclei (Figure10(c)) [83]. The TiO_2 nuclei grow and cover the surface of α-Ti with continuous supply of Ti^{4+} and OH^- ions (Figure 10(c)). Hydrogen evolves as a byproduct of the reactions [83]. When the surface is fully covered with TiO_2 layer, oxygen ions start to diffuse inward via grain boundaries and reacts with Ti ions beneath the newly formed TiO_2 layer [81, 82]. Lower valence oxide such as, Ti_3O_5 is formed at this stage of oxidation as shown in Figure 10(d).

Previously similar phenomena, i.e., the presence of multilayered oxides were observed during oxidation of Cu and Fe substrates for the growth of 1D CuO [57-59] and Fe_2O_3 [60-62] nanostructures, respectively. It was proposed by Kumar *et al*. [57] that stress is induced during oxidation of Cu substrate between the formed oxide layers of CuO and Cu_2O. This induced stress is compensated by forming new surfaces in the form of 1D CuO nanostructures during oxidation [57]. Similar scenario is proposed in the present case during humid oxidation of Ti, where multilayered oxides are seen in XRD (Figure 6(b)), XPS (Figure7) and EDX (Figure 8) analysis. It should be noted that during humid oxidation of Ti, rutile TiO_2 forms at the outermost layer which has tetragonal crystal structure. Beneath, rutile TiO_2, monoclinic Ti_3O_5 is formed. Due to difference in crystal structures, densities and molar volumes, it is expected that substantial stress is induced at the TiO_2-Ti_3O_5 interface. Diffusion of oxygen at the interface of TiO_2-Ti_3O_5 also accumulates stress [57]. Due to difference in concentration, Ti^{4+} ions diffuse interstitially from the substrate to the top surface of TiO_2 layer and react with surface absorbed OH^-. As long as the oxidation process continues, stress is accumulated at the interface and after reaching a critical limit the oxide layer relaxes the induced stress by forming TiO_2 nuclei of 1D nanostructure on existing TiO_2 grains (Figure 10(d)). It is thermodynamically more viable to form nuclei of 1D nanostructures on existing TiO_2 grains as it does not require to overcome the energy barrier for nucleation [58]. The nuclei of TiO_2 grows longer by continuous diffusion of Ti^{4+} ions via interstitial sites and reacts with surface adsorbed OH^- ions (Figure 10(e-f)). On the other hand, oxygen ions diffuse via grain boundaries and reacts with Ti ions to form rhombohedral Ti_2O_3 and face centered cubic TiO at the oxide-metal interface at the later stages of oxidation (Figure 10(e-f)). In the presence of limited supply of oxygen, the growth of as-grown TiO_2 nuclei occur along <1 0 1> directions resulting in 1D TiO_2 nanostructures [51]. At high

concentration of oxygen, the growth of nuclei occurs in all directions and as a result oxide scale is seen instead of 1D nanostructures.

Besides the induced stress, ball milling or other means of cold working also impose stress on Ti substrates. During humid oxidation, additional residual stress imposed by cold working on Ti releases by enhancing new surfaces in the form of 1D TiO_2 nanostructures. For this reason, high coverage of 1D TiO_2 nanostructures is seen in the milled particles compared with the as-received particles.

So, during humid oxidation, 1D TiO_2 nanostructures form on TiO_2 layer by the reaction between surface adsorbed OH^- ion and interstitially diffused $Ti4^+$ ions. Lower valence of oxides of Ti forms beneath the TiO_2 layer due to grain boundary diffusion of oxygen ions. In the literature, different environments such as CH_3COCH_3 [31, 45-47], C_2H_5OH [47, 49, 50], CH_3CHO [47] and $C_{32}H_{64}O_4Sn$ [48] in Ar was used as oxidizing medium for the growth of 1D TiO_2 on Ti substrates (Table 2). Out of these, humid Ar environment is an easy, low-cost and affordable oxidizing medium to obtain good coverage of 1D TiO_2 nanostructures.

Table 2: Summary of the 1D nanostructures grown by thermal oxidation process on Ti substrates.

Nanostructure	Substrate, dimensions and source	Oxidation environment	Growth temperature (°C)	Growth time	Dimension of the 1-D nanostructures	Crystal structure	Growth direction	Reference
1D TiO_2 nanostructures	Ti particles (as-received and milled), Ti plate and Ti TEM grid	5 ppm O_2 in humid Ar	700-750 °C	4 h	Thickness: 50-500 nm Length: 5 -10 µm	Rutile	<1 0 1>	Present work
TiO_2 nanowires	Ti foil	Acetone vapor in Ar	800°C	1 h	Diameter: 20-50 nm	Rutile	-	[45]
TiO_2 nanorods	Ti plate	Acetone vapor in Ar	850 °C	1.5 h	Tetragonal structure: Width: ~1.5 µm Thickness: 100 nm Length: 1-2 µm Columnar structure: Diameter: 230 nm Length: 2-3 µm	Rutile	[0 0 1]	[46, 47]
Core-shell TiO_2-C	Ti foil	Acetone vapor in Ar	850°C	1.5 h	Diameter: 15-20 nm	Rutile	[1 01]	[31]
TiO_2 plate-like nanostrcutres	Ti plate	Ethanol vapor in Ar	850 °C	1.5 h	Width: 500 nm Thickness: 150 nm Length: 1 µm	Rutile	-	[47]
TiO_2 nanowire	Ti particles	Ethanol	650-800 °C	30-180 min	Diameter: 60-150 nm Length: ~2 µm	Rutile	-	[49]
TiO_2 nanowire	Ti wire	Ethanol	650-850 °C	30-180 min	Diameter: 23-73 nm	Rutile	[0 0 1]	[50]
TiO_2 nanorods	Ti plate	Acetaldehyde vapor in Ar	850 °C	1.5 h	Width: 500 nm Thickness: 150 nm Length: 1 µm	Rutile	-	[47]
TiO_2 nanorods	Ti plate	Dibutyltin dilaurate in Ar	600-900 °C	4 h	Width: 150 nm Length: several hundred nanometer Height: 1.5 µm	Rutile	[0 0 1]	[48]
TiO_2 nanofibers	Ti plate	Mixture of Ar and O_2	850 °C	1.5 h	Chain-like structure: Diameter: 200 nm Length: several micrometers Ribbon-like structure: Width: 200-1500 nm Thickness: 60 nm Length: several micrometers	Rutile	[0 0 1]	[46]

*Different terminologies were used in the literature interchangeably to describe 1D TiO_2 based nanostructures. To avoid confusion, the term "1D nanostructures" is explicitly used in this article. However, the original terminologies used in the literatures are preserved in Table 2.

Our present study clearly demonstrates that residual stress imposed by ball milling enhances the growth of 1D TiO_2 nanostructures on Ti substrate during thermal oxidation. Different morphological variations are observed during oxidation of Ti substrates. The 1D nanostructures and underlying oxide scales are characterized. From the results a probable diffusion based growth model is proposed.

4. Conclusions

Thermal oxidation is a simple, inexpensive, catalyst-free and scalable method for synthesizing one dimensional (1D) TiO_2 nanostructures on Ti substrates. This process requires heating the Ti substrates in oxygen containing humid environment. Both residual stress and induced stress play role during oxidation for the formation of 1D TiO_2 nanostructures. The following conclusions are drawn from this present work.

1. The presence of humid environment is essential for the growth of 1D TiO_2 nanostructures. Dry oxidation resulted in oxide scale with very low coverage of 1D nanostructures.
2. Four types of morphological variations such as stacked, ribbon, plateau and lamp-post shaped TiO_2 nanostructures are seen on oxidized Ti substrates. However, the prevalence of stacked nanostructures is most abundant. The 1D TiO_2 nanostructures are single crystalline and possess tetragonal rutile structure. The 1D TiO_2 nanostructures grow along <1 0 1> directions.
3. During humid oxidation TiO_2 layers is formed beneath the 1D nanostructures. Lower valence oxides such as Ti_3O_5, Ti_2O_3 and TiO forms underneath the TiO_2 layer.
4. Residual stress imposed by ball milling significantly increases the coverage of 1D TiO_2 nanostructures during oxidation. The residual stress is compensated during oxidation by creating new surfaces in the form of 1D TiO_2 nanostructures.
5. A diffusion based model is proposed for the formation of 1D TiO_2 nanostructures on Ti substrates during humid oxidation. It is proposed that the Ti^{4+} ions diffuse interstitially and reacts with surface adsorbed hydroxide ions to form TiO_2 layer and 1D TiO_2 nanostructures. On the other hand, oxygen ions diffuse through grain boundaries and react with Ti ions to form lower valence oxides such as Ti_3O_5, Ti_2O_3, TiO at the metal-oxide interface.

Acknowledgements

The authors would like to acknowledge the financial support from Impact-oriented Interdisciplinary Research Grant (Project No.: IIRG018C-2019) of University of Malaya and Marie Skłodowska-Curie Individual Fellowships (Project No.: 898736) from European Commission Research Executive Agency.

References

[1] A.K. Mahapatra, Synthesis of quantum-confined CdS nanotubes, Journal of Nanoparticle Research, 11 (2009) 467-475.

[2] M.M.G. Alemany, L. Tortajada, X.Y. Huang, M.L. Tiago, L.J. Gallego, J.R. Chelikowsky, Role of dimensionality and quantum confinement in p-type semiconductor indium phosphide quantum dots, Physical Review B, 78 (2008) 233101.

[3] P.J. Poole, J. Lefebvre, J. Fraser, Spatially controlled, nanoparticle-free growth of InP nanowires, Applied Physics Letters, 83 (2003) 2055-2057.

[4] P. Keller, H. Ferkel, K. Zweiacker, J. Naser, J.U. Meyer, W. Riehemann, The application of nanocrystalline $BaTiO_3$-composite films as CO_2-sensing layers, Sensors and Actuators B: Chemical, 57 (1999) 39-46.

[5] M. Shafiei, J. Yu, R. Arsat, K. Kalantar-zadeh, E. Comini, M. Ferroni, G. Sberveglieri, W. Wlodarski, Reversed bias Pt/nanostructured ZnO Schottky diode with enhanced electric field for hydrogen sensing, Sensors and Actuators B: Chemical, 146 (2010) 507-512.

[6] H.W. Peng, J.B. Li, Quantum confinement and electronic properties of rutile TiO_2 nanowires, Journal of Physical Chemistry C, 112 (2008) 20241-20245.

[7] P.V. Avramov, D.G. Fedorov, P.B. Sorokin, L.A. Chernozatonskii, S.G. Ovchinnikov, Quantum dots embedded into silicon nanowires effectively partition electron confinement, Journal of Applied Physics, 104 (2008) 054305.

[8] E.D. Herderick, J.S. Tresback, A.L. Vasiliev, N.P. Padture, Template-directed synthesis, characterization and electrical properties of Au-TiO_2-Au heterojunction nanowires, Nanotechnology, 18 (2007) 155204.

[9] Y. Huang, X.F. Duan, Y. Cui, C.M. Lieber, Gallium nitride nanowire nanodevices, Nano Letters, 2 (2002) 101-104.

[10] Y.L. Chueh, C.H. Hsieh, M.T. Chang, L.J. Chou, C.S. Lao, J.H. Song, J.Y. Gan, Z.L. Wang, RuO_2 nanowires and RuO_2/TiO_2 core/shell nanowires: From synthesis to mechanical, optical, electrical, and photoconductive properties, Advanced Materials, 19 (2007) 143-149.

[11] Y. Xia, P. Yang, Y. Sun, Y. Wu, B. Mayers, B. Gates, Y. Yin, F. Kim, H. Yan, One-dimensional nanostructures: synthesis, characterization, and applications, Advanced Materials, 15 (2003) 353-389.

[12] T.-Y. Tsai, S.-J. Chang, T.-J. Hsueh, H.-T. Hsueh, W.-Y. Weng, C.-L. Hsu, B.-T. Dai, p-Cu_2O-shell/n-TiO_2-nanowire-core heterostucture photodiodes, Nanoscale Research Letters, 6 (2011) 575.

[13] S. Ni, D. Wang, F. Guo, S. Jiao, Y. Zhang, J. Wang, B. Wang, L. Yuan, L. Zhang, L. Zhao, Efficiency improvement of TiO_2 nanowire arrays based dye-sensitized solar cells through further enhancing the specific surface area, Journal of Crystal Growth, 505 (2019) 62-68.

[14] P. Makal, D. Das, Graphitic carbon nitride (g-C_3N_4) incorporated TiO_2-B nanowires as efficient photoanode material in dye sensitized solar cells, Materials Chemistry and Physics, 266 (2021) 124520.

[15] P. Pooja, P. Chinnamuthu, Annealed n-TiO_2/In_2O_3 nanowire metal-insulator-semiconductor for highly photosensitive low-noise ultraviolet photodetector, Journal of Alloys and Compounds, 854 (2021) 157229.

[16] R. Lahiri, A. Ghosh, B. Choudhuri, A. Mondal, Investigation on improved performance of Erbium doped TiO_2 nanowire based UV detector, Materials Research Bulletin, 103 (2018) 259-267.

[17] L.A. Al-Hajji, A. A..Ismail, A. Al-Hazza, S.A. Ahmed, M. Alsaidi, F. Almutawa, A. Bumajdad, Impact of calcination of hydrothermally synthesized TiO_2 nanowires on their photocatalytic efficiency, Journal of Molecular Structure, 1200 (2020) 127153.

[18] H. Tu, D. Li, Y. Yi, R. Liu, Y. Wu, X. Dong, X. Shi, H. Deng, Incorporation of rectorite into porous polycaprolactone/TiO_2 nanofibrous mats for enhancing photocatalysis properties towards organic dye pollution, Composites Communications, 15 (2019) 58-63.

[19] S.T. Rahmat, W.K. Tan, G. Kawamura, A. Matsuda, Z. Lockman, Synthesis of rutile TiO_2 nanowires by thermal oxidation of titanium in the presence of KOH and their ability to photoreduce Cr(VI) ions, Journal of Alloys and Compounds, 812 (2020) 152094.

[20] X. Hou, S. Jiang, Y. Li, A two-anode reduction technique to monitor the defect and dope the surface of TiO_2 nanotube array as photo-anode for water splitting, Applied Catalysis B: Environmental, 258 (2019) 117949.

[21] R. Zhang, M. Shao, S. Xu, F. Ning, L. Zhou, M. Wei, Photo-assisted synthesis of zinc-iron layered double hydroxides/TiO_2 nanoarrays toward highly-efficient photoelectrochemical water splitting, Nano Energy, 33 (2017) 21-28.

[22] B.J. Rani, M. Praveenkumar, S. Ravichandran, V. Ganesh, R.K. Guduru, G. Ravi, R. Yuvakkumar, Ultrafine M-doped TiO_2 (M = Fe, Ce, La) nanosphere photoanodes for photoelectrochemical water-splitting applications, Materials Characterization, 152 (2019) 188-203.

[23] Y. Sun, K.-P. Yan, Effect of anodization voltage on performance of TiO_2 nanotube arrays for hydrogen generation in a two-compartment photoelectrochemical cell, International Journal of Hydrogen Energy, 39 (2014) 11368-11375.

[24] K. Shin, S.I. Seok, S.H. Im, J.H. Park, CdS or CdSe decorated TiO_2 nanotube arrays from spray pyrolysis deposition: use in photoelectrochemical cells, Chemical Communications, 46 (2010) 2385-2387.

[25] M.M. Arafat, A.S.M.A. Haseeb, S.A. Akbar, M.Z. Quadir, In-situ fabricated gas sensors based on one dimensional core-shell TiO_2-Al_2O_3 nanostructures, Sensors and Actuators B: Chemical, 238 (2017) 972-984.

[26] M. Zhou, Y. Liu, B. Wu, X. Zhang, Different crystalline phases of aligned TiO_2 nanowires and their ethanol gas sensing properties, Physica E: Low-dimensional Systems and Nanostructures, 114 (2019) 113601.

[27] J.M. Macak, C. Zollfrank, B.J. Rodriguez, H. Tsuchiya, M. Alexe, P. Greil, P. Schmuki, Ordered ferroelectric lead titanate nanocellular structure by conversion of anodic TiO_2 nanotubes, Advanced Materials, 21 (2009) 3121-3125.

[28] H. Zheng, T. Zhai, M. Yu, S. Xie, C. Liang, W. Zhao, S.C.I. Wang, Z. Zhang, X. Lu, TiO_2@C core-shell nanowires for high-performance and flexible solid-state supercapacitors, Journal of Materials Chemistry C, 1 (2013) 225-229.

[29] C. Li, Y. Huang, C. Chen, X. Feng, Z. Zhang, High-performance polymer electrolyte membrane modified with isocyanate-grafted Ti^{3+} doped TiO_2 nanowires for lithium batteries, Applied Surface Science, 563 (2021) 150248.

[30] X. Lu, F. Luo, Q. Tian, W. Zhang, Z. Sui, J. Chen, Anatase TiO_2 nanowires intertangled with CNT for conductive additive-free lithium-ion battery anodes, Journal of Physics and Chemistry of Solids, 153 (2021) 110037.

[31] K. Huo, X. Zhang, L. Hu, X. Sun, J. Fu, P.K. Chu, One-step growth and field emission properties of quasialigned TiO_2 nanowire/carbon nanocone core-shell nanostructure arrays on Ti substrates, Applied Physics Letters, 93 (2008) 013105.

[32] T. Zhang, C. Chen, Z. Liang, L. Wang, F. Gao, W. Yang, S. Chen, Boosting field emission performance of TiO_2 nanoarrays with designed architectures, Applied Surface Science, 507 (2020) 145146.

[33] S. Saha, K. Pramanik, A. Biswas, Silk fibroin coated TiO_2 nanotubes for improved osteogenic property of Ti6Al4V bone implants, Materials Science & Engineering C, 105 (2019) 109982.

[34] A.W. Tan, B. Pingguan-Murphy, R. Ahmad, S.A. Akbar, Review of titania nanotubes: fabrication and cellular response, Ceramics International, 38 (2012) 4421-4435.

[35] C.S. Rout, G. U.Kulkarni, C.N.R. Rao, Room temperature hydrogen and hydrocarbon sensors based on single nanowires of metal oxides, Journal of Physics D: Applied Physics, 40 (2007) 2777-2782.

[36] C.-H. Han, D.-W. Hong, I.-J. Kim, J. Gwak, S.-D. Han, K.C. Singh, Synthesis of Pd or Pt/titanate nanotube and its application to catalytic type hydrogen gas, Sensors and Actuators B: Chemical, 128 (2007) 320-325.

[37] O. Landau, A. Rothschild, E. Zussman, Processing-microstructure-properties correlation of ultrasensitive gas sensors produced by electrospinning, Chemistry of Materials, 21 (2009) 9-11.

[38] W. Biao, Z. Y.Dong, H.L. Ming, C.J. Sheng, G.F. Li, L. Yun, W.L. Jun, Improved and excellent CO sensing properties of Cu-doped TiO_2 nanofibers, Chinese Science Bulletin, 55 (2010) 228-232.

[39] A. Hu, C. Cheng, X. Li, J. Jiang, R. Ding, J. Zhu, F. Wu, J. Liu, X. Huang, Two novel hierarchical homogeneous nanoarchitectures of TiO_2 nanorods branched and P25-coated TiO_2 nanotube arrays and their photocurrent performances, Nanoscale Research Letters, 6 (2011) 2-6.

[40] H.F. Lu, F. Li, G. Liu, Z.-G.Chen, D.-W. Wang, H.-T. Fang, G.Q. Lu, Z.H. Jiang, H.-M. Cheng, Amorphous TiO_2 nanotube arrays for low-temperature oxygen sensors, Nanotechnology, 19 (2008) 405504.

[41] M. Paulose, O.K. Varghese, G.K. Mor, C.A. Grimes, K.G. Ong, Unprecedented ultra-high hydrogen gas sensitivity in undoped titania nanotubes, Nanotechnology, 17 (2006) 398-402.

[42] S. Yoo, S.A. Akbar, K.H. Sandhage, Nanocarving of titania (TiO_2): a novel approach for fabricating chemical sensing platform, Ceramics International, 30 (2004) 1121-1126.

[43] C.M. Carney, S. Yoo, S.A. Akbar, TiO_2-SnO_2 nanostructures and their H_2 sensing behavior, Sensors and Actuators B: Chemical, 108 (2005) 29-33.

[44] L. Francioso, A.M. Taurino, A. Forleo, P. Siciliano, TiO_2 nanowires array fabrication and gas sensing properties, Sensors and Actuators B: Chemical, 130 (2008) 70-76.

[45] K. Huo, X. Zhang, J. Fu, G. Qian, Y. Xin, B. Zhu, H. Ni, P.K. Chu, Synthesis and field emission properties of rutile TiO_2 nanowires arrays grown directly on a Ti metal self-source substrate, Journal of Nanoscience and Nanotechnology, 9 (2009) 3341-3346.

[46] X. Peng, A. Chen, Aligned TiO_2 nanorod arrays synthesized by oxidizing titanium with acetone, Journal of Materials Chemistry, 14 (2004) 2542-2548.

[47] X. Peng, J. Wang, D.F. Thomas, A. Chen, Tunable growth of TiO_2 nanostructures on Ti substrates, Nanotechnology, 16 (2005) 2389-2395.

[48] X. Peng, A. Chen, Dense and high-hydrophobic rutile TiO_2 nanorod arrays, Applied Physics A, 80 (2005) 473-476.

[49] D. Kaewsai, W. Jaruwongjinda, S. Daothong, P. Singjai, A. Watcharapasorn, S. Jiansirisomboon, Phase and microstructure of TiO_2 nanowires synthesized by thermal oxidation, Journal of the Microscopy Society of Thailand, 24 (2010) 145-148.

[50] S. Daothong, N. Songmee, S. Thongtem, P. Singjai, Size-controlled growth of TiO_2 nanowires by oxidation of titanium substrates in the presence of ethanol vapor, Scripta Materialia, 57 (2007) 567-570.

[51] H. Lee, S. Dregia, S. Akbar, M. Alhoshan, Growth of 1-D TiO_2 nanowires on Ti and Ti alloys by oxidation, Journal of Nanomaterials, 2010 (2010) Article ID 503186.

[52] M.M. Arafat, A.S.M.A. Haseeb, B. Dinan, S.A. Akbar, Stress enhanced TiO_2 nanowire growth on Ti-6Al-4V particles by thermal oxidation, Ceramics International, 39 (2013) 6517-6526.

[53] M.M. Arafat, A.S.M.A. Haseeb, S.A. Akbar, Growth and characterization of the oxide scales and core/shell nanowires on Ti-6Al-4V particles during thermal oxidation, Ceramics International, 41 (2015) 4401-4409.

[54] B. Dinan, S.A. Akbar, One-dimensional oxide nanostructures produced by gas phase reaction, Functional Materials Letters, 2 (2009) 87-94.

[55] I. Lee, Carbon dioxide resistive sensor based on titanium oxide nanowires doped with potassium, Micro & Nano Letters, 9 (2014) 248-250.

[56] K.Y. Cheung, C.T. Yip, A.B. Djurišić, Y.H. Leung, W.K. Chan, Long K-doped titania and titanate nanowires on Ti foil and fluorine-doped tin oxide/quartz substrates for solar-cell applications, Advanced Functional Materials, 17 (2007) 555-562.

[57] A. Kumar, A.K. Srivastava, P. Tiwari, R.V. Nandedkar, The effect of growth parameters on the aspect ratio and number density of CuO nanorods, Journal of Physics: Condensed Matter, 16 (2004) 8531-8543.

[58] L. Yuan, Y. Wang, R. Mema, G. Zhou, Driving force and growth mechanism for spontaneous oxide nanowire formation during the thermal oxidation of metals, Acta Materialia, 59 (2011) 2491-2500.

[59] L. Yuan, G. Zhou, Enhanced CuO nanowire formation by thermal oxidation of roughened copper, Journal of the Electrochemical Society, 159 (2012) C205-C209.

[60] A.G. Nasibulin, S. Rackauskas, H. Jiang, Y. Tian, P.R. Mudimela, S.D. Shandakov, L.I. Nasibulina, J. Sainio, E.I. Kauppinen, Simple and rapid synthesis of α-Fe_2O_3 nanowires under ambient conditions, Nano Research, 2 (2009) 373-379.

[61] L. Yuan, Y. Wang, R. Cai, Q. Jiang, J. Wang, B. Li, A. Sharma, G. Zhou, The origin of hematite nanowire growth during the thermal oxidation of iron, Materials Science and Engineering B, 177 (2012) 327-336.

[62] L. Yuan, R. Cai, J.I. Jang, W. Zhu, C. Wang, Y. Wang, G. Zhou, Morphological transformation of hematite nanostructures during oxidation of iron, Nanoscale, 5 (2013) 7581-7588.

[63] R. Mema, L. Yuan, Q. Du, Y. Wang, G. Zhou, Effect of surface stresses on CuO nanowire growth in the thermal oxidation of copper, Chemical Physics Letters, 512 (2011) 87-91.

[64] B.J. Hansen, H.-L. Chan, J. Lu, G. Lu, J. Chen, Short-circuit diffusion growth of long bi-crystal CuO nanowires, Chemical Physics Letters, 504 (2011) 41-45.

[65] L.-B. Luo, X.-H. Wang, C. Xie, Z.-J. Li, R. Lu, X.-B. Yang, J. Lu, One-dimensional CuO nanowire: synthesis, electrical, and optoelectronic devices application, Nanoscale Research Letters, 9 (2014) 637.

[66] V.M. Hauk, X-ray methods for measuring residual stress, In: Residual stress and stress relaxation, E. Kula, V. Weiss (Eds.), Sagamore Army Materials Research Conference Proceedings, Lake Placid, Plenum Press, NY, (1982).

[67] B.D. Cullity, S.R. Stock, Elements of X-ray diffraction, 3rd Edition, Prentice Hall, Upper Saddle River, NJ, (2001).

[68] M.E. Fitzpatrick, A.T. Fry, P. Holdway, F.A. Kandil, J. Shackleton, L. Suominen, Determination of residual stresses by X-ray diffraction-Issue 2, DTI, Measurement Good Practice Guide No. 52, (2005).

[69] W.H. Bragg, W.L. Bragg, The reflection of X-rays by crystals, Proceedings of the Royal Society of London, Series A, 88 (1913) 428-438.

[70] P.S. Prevéy, X-ray diffraction residual stress techniques, ASM International, ASM Handbook, 10 (1986) 380-392.

[71] S. Kurajica, E. Tkalčec, G. Matijašić, L. Ćurković, Z. Schauperl, J. Šipušić, V. Mandić, Influence of agglomeration and contamination in the course of amorphous powder grinding on structure and microstructure of sintered mullite, Croatica Chemica Acta, 84 (2011) 63-71.

[72] X. Zheng, J. Li, Y. Zhou, X-ray diffraction measurement of residual stress in PZT thin films prepared by pulsed laser deposition, Acta Materialia, 52 (2004) 3313-3322.

[73] Q. Luo, A.H. Jones, High-precision determination of residual stress of polycrystalline coatings using optimised XRD-$\sin^2\psi$ technique, Surface & Coatings Technology, 205 (2010) 1403-1408.

[74] M.M. Arafat, S. Rozali, A.S.M.A. Haseeb, S. Ibrahim, Direct and catalyst-free synthesis of ZnO nanowires on brass by thermal oxidation, Nanotechnology, 31 (2020) 175603.

[75] G. Lu, S.L. Bernasek, J. Schwartz, Oxidation of a polycrystalline titanium surface by oxygen and water, Surface Science, 458 (2000) 80-90.

[76] A.G.Y. Wouters, J.-P. Petit, Interfacial reactions and diffusion during the thermal oxidation of titanium in water vapour, Materials Science Forum, 251-254 (1997) 113-118.

[77] P. Pérez, On the influence of water vapour on the oxidation behaviour of pure Ti, Corrosion Science, 49 (2007) 1172-1185.

[78] M.C. Biesinger, L.W.M. Lau, A.R. Gerson, R.S.C. Smart, Resolving surface chemical states in XPS analysis of first row transition metals, oxides and hydroxides: Sc, Ti, V, Cu and Zn, Applied Surface Science, 257 (2010) 887-898.

[79] A.F. Carley, J.C. Roberts, M.W. Roberts, Dissociative chemisorption and localized oxidation states at titanium surfaces, Surface Science Letters, 225 (1990) L39-L41.

[80] B. Erdem, R.A. Hunsicker, G.W. Simmons, E.D. Sudol, V.L. Dimonie, M.S. El-Aasser, XPS and FTIR surface characterization of TiO_2 particles used in polymer encapsulation, Langmuir, 17 (2001) 2664-2669.

[81] J. Stringer, The oxidation of titanium in oxygen at high temperatures, Acta Metallurgica, 1960 (1960) 758-766.

[82] S. Taniguchi, N. Hongawara, T. Shibata, Influence of water vapour on the isothermal oxidation behaviour of TiAl at high temperatures, Materials Science and Engineering A, 307 (2001) 107-112.

[83] A. Galerie, Y. Wouters, J.-P. Petit, Interfacial reactions and diffusion during the thermal oxidation of titanium in water vapour, Materials Science Forum, 251-254 (1997) 113-118.